IIETA International Information and Engineering Technology Association
Advancing the World of Information and Engineering

Instrumentation Mesure Métrologie
Vol. 25, No. 2, April, 2026, pp. 51-59
Journal homepage: http://iieta.org/journals/i2m

Design and Manufacture of a Stand for Measuring the Illuminance Differences of Semi-Transparent Materials Used in Additive Manufacturing

Kliment K. Georgiev[1*], Misho Iv. Matsankov[2], Atanas P. Radulov[2], Mario T. Dechev[2], Teodor V. Demirev[1]

[1] Department of Instrumentation and Mechanical Engineering, Technical University of Sofia, Plovdiv 4000, Bulgaria
[2] Department of Electrical Engineering, Technical University of Sofia, Plovdiv 4000, Bulgaria

Corresponding Author Email: k.georgiev@tu-plovdiv.bg

https://doi.org/10.18280/i2m.250201

Received: 9 February 2026
Revised: 23 March 2026
Accepted: 2 April 2026
Available online: 30 April 2026

Keywords:
additive manufacturing, data collection system, light transmittance, semi-transparent materials, stand design, fused deposition modeling

ABSTRACT

The article presents the design and construction of a stand for measuring the transmittance of semi-transparent materials used in additive manufacturing. It also describes an automated system for the control of measurement processes and the collection of data. The platform is built around an ESP32-based controller programmed via the Arduino Integrated Development Environment (IDE). The system integrates a light sensor for transmitted-light measurements, temperature sensors for tracking ambient and/or module temperatures, a controlled light source, Pulse-Width Modulation (PWM) drivers for light-source regulation, and a dedicated module for the measurement of electrical quantities associated with the illumination and control subsystems. The designed stand was fabricated by additive printing technologies, subsequently assembled, and then tested in a controlled laboratory environment. The measurement data are presented herein to validate the stand's operability. The stand demonstrates stable operation, high repeatability of measurements, and the possibility of quick readjustment. Its modular design enables quick replacement of the light source and test specimens, supporting a broader range of experimental studies.

1. INTRODUCTION

Additive manufacturing by fused deposition modeling (FDM), also known as fused filament fabrication (FFF), has transitioned from rapid prototyping to functional production of components for consumer, lighting, and optical applications. A growing subset of applications exploits translucent FDM parts, e.g., lampshades, diffusers, light covers, and housing, where controlled light transmission and scattering are central to performance rather than an incidental byproduct of the process [1-3]. For such components, designers require quantitative knowledge of visible-range light transport: not only spectral transmittance, but also luminous transmittance, haze, and the balance between regular (collimated) and diffuse transmission.

In conventional polymer optics, these quantities are routinely characterized with spectrophotometers equipped with integrating spheres under standards such as ASTM D1003 and ISO 13468. These standards prescribe measurement geometry, wavelength range, sphere design, and sample preparation for transparent and translucent plastic sheets. Recent metrology work has refined and critiqued these procedures, highlighting the importance of integrating-sphere geometry, port fraction, and measurement mode (single- vs. double-beam; single- vs. double-compensation) for accurate and traceable measurements of total luminous transmittance and haze [4-6]. Parallel efforts in color and appearance science have leveraged integrating-sphere data to infer intrinsic optical parameters—absorption and scattering coefficients, phase functions, and refractive index—of translucent polymers using radiative-transfer models and machine-learning inversion [7-9].

These established approaches cannot, however, be transferred naively to FDM-produced translucent parts. FDM microstructure is highly heterogeneous and anisotropic: extruded filaments form roads with inter-road and inter-layer voids, partial coalescence zones, and surface stair-stepping, all embedded in a semi-crystalline or amorphous polymer matrix. The resulting refractive-index fluctuations and void distributions generate strong multiple scattering, often dominating bulk absorption in determining the overall transmittance and appearance of the part. Hamp et al. [3] demonstrated that transmittance of 3D-printed materials as a function of thickness departs markedly from simple Beer–Lambert behavior due to multiple scattering, even for relatively simple multithickness specimens measured in a direct-beam geometry. This indicates that standard homogeneous-slab assumptions, underlying much of traditional optical characterization, are at best approximate for typical FDM plaques.

Only a small number of studies have directly addressed the optical characterization of FDM-printed translucent parts using sphere-based methods. Wang and Zhou [1] printed flat polylactic acid (PLA) plaques intended for lampshade

applications and measured their spectral transmittance and haze with a commercial UV–Vis spectrophotometer equipped with an integrating sphere, explicitly referencing ISO 14782:2021 for haze determination. They systematically investigated the influence of color (milky vs. colorless PLA), wall thickness, and layer height, showing that milky PLA acts as a stronger diffuser with better luminous uniformity, and that increasing wall thickness reduces transmittance while increasing haze [1]. Vochozk et al. [2] used an integrating sphere with a luxmeter to quantify the "translucency" (essentially luminous total transmittance) of PLA plaques as a function of six FFF processing parameters—orientation, layer height, nozzle temperature, fan speed, extrusion multiplier, and print speed—across 32 parameter combinations and ten replicates each. All investigated factors were found to significantly affect the measured luminous transmittance, underscoring the sensitivity of optical behavior to FDM process settings [2].

These FDM-focused works, however, do not yet amount to a comprehensive, standards-like methodology for visible-range total transmittance of FDM translucent parts. Instrument geometry and port fractions are only partially documented [1, 2], and there is limited discussion of how deviations from the flat, polished, homogeneous sheets assumed in ISO/ASTM methods—e.g., surface relief from layer lines, internal porosity, and anisotropic road patterns—should be handled in sample preparation, alignment, and data interpretation. At the same time, the broader metrology literature makes clear that integrating-sphere design and operating mode can introduce systematic biases in total transmittance and haze. Shahpaski et al. [4] demonstrated, with a flexible custom integrating-sphere bench, that different illumination/collection geometries (0°/d, d/d, d/0°), port arrangements, and detector fields-of-view produce measurable shifts in total transmittance and haze compared to commercial instruments and provided detailed design guidelines for achieving comparability with ASTM D1003-type measurements. Hwang and Baek [5] recently showed analytically and experimentally that standard single-beam sphere methods, as recommended in ASTM and ISO standards, retain multiplicative factors from multiple reflections in the sphere, whereas a double-beam configuration can cancel these factors and reduce bias in luminous transmittance and haze. An inter-laboratory pilot comparison coordinated within the Asia Pacific Metrology Programme further confirmed that double-beam and double-compensation methods provide more consistent total and diffuse transmittance than conventional ASTM D1003 implementations, even for high-transmittance artefacts [6].

In parallel, appearance-oriented research on 3D-printing materials has advanced the use of standard reflectance/transmittance spectrophotometers, often with integrating spheres, to recover intrinsic optical properties rather than just phenomenological transmittance values. Simonot et al. [7] combined sphere measurements of slightly scattering polymer sheets with an extended two-flux radiative-transfer model to separate regular and diffuse components and to predict the reflectance and transmittance of stacked layers. More recently, Pranovich et al. [9] proposed printing collections of slabs with different thicknesses, measuring their sphere-based reflectance and transmittance, and fitting analytic or Monte Carlo radiative-transfer models to estimate scattering and absorption coefficients for appearance prediction of 3D-printed parts. Abu Rmaileh et al. [8] extended this idea by modelling the light paths inside a commercial reflectance/transmittance spectrophotometer via Monte Carlo simulation and training machine-learning models to invert measured R/T spectra to absorption, scattering, phase function, and refractive index of printing materials, demonstrating agreement with independent laboratory-grade measurements.

Taken together, these strands of research suggest both an opportunity and a need. On the one hand, FDM studies show that process parameters can be tuned to achieve specific levels of luminous transmittance and scattering in translucent parts [1-3]. On the other hand, integrating-sphere metrology and appearance modeling provides the tools to rigorously quantify total transmittance, diffuse/regular components, and even intrinsic optical coefficients in translucent polymers [4-10]. Yet there is, to date, no unified, FDM-specific framework that adapts sphere-based standards, bench design, and inversion methodologies to the particular microstructural realities of FDM-printed translucent components.

In recent years, additive manufacturing (3D printing) has seen a marked increase in its use for the rapid and straightforward production of functional prototypes. The manufacturing process is distinguished by the wide array of materials used, as well as their specific properties and characteristics. A significant corpus of scientific studies is dedicated to the mechanical and geometric properties of the materials utilised in this production, as well as to the technological factors influencing the production process. However, research on the light transmittance of semi-transparent materials for additive printing remains scarce. The purpose of this article is to present a designed and manufactured stand for measuring the permeability of translucent materials used in additive manufacturing. The design of the test stand arose from the idea of researching translucent materials and their potential applications in various industries (automotive manufacturing, advertising, and lighting fixture production). The low cost of additive manufacturing and the availability of components (sensors, microcontrollers, and other parts) made it possible to build the stand shown here. The test samples and their holders are manufactured according to the needs of the research.

2. MATERIALS AND METHODS

This section presents a 3D model of the stand, manufacturing technology, materials used for manufacturing, printing parameters and conditions, and the main components of the control and measurement system.

2.1 3D model of the stand

When designing the stand for measuring the transmittance of translucent materials, several basic principles for measuring light transmittance are followed. A high-power LED with a beam angle of 30° was used as the light source, as shown in Figure 1. A diameter of Ø45 mm is selected for the test objects. This diameter allows for the design of a compact stand, lower filament consumption for the production of test details, easier operation, and good layer formation. Based on the angle of radiation and the diameter of the test object, the distance from the light source to the object is calculated, which in this case is 83.97 mm. The diagram according to which the stand is designed is shown in Figure 1.

Preliminary assessments and the ensuing findings, illustrated in Figure 1, have guided the conceptualisation of a three-dimensional model of the stand. The model is delineated as follows: (1) denotes the base, (2) signifies the removable cover, (3) designates the holder for the tested object, and (4) represents the holder for the light sensor. Please refer to Figure 2. The light source is positioned on the base of the stand. The stand features a modular design, allowing different LED light sources to be used. The test object is to be placed in holder 3. The holder and the test object are then to be placed on the base of the stand, after which a removable cover is to be used to cover both the holder and the test object. Sensor 4 is then to measure the illuminance and transmit the resulting data to the central processor.

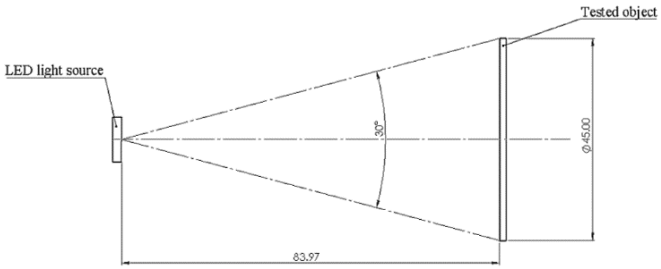

Figure 1. Distance scheme: Light source–tested object

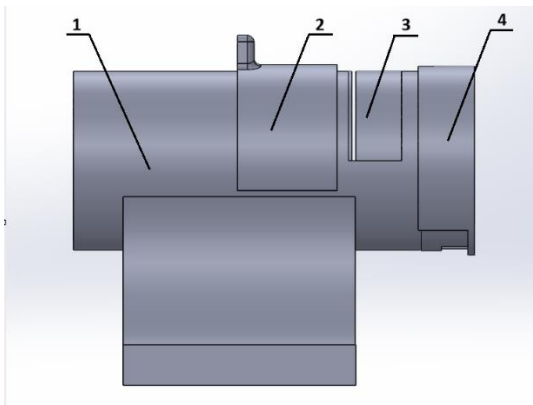

Figure 2. 3D model of the stand

In order to ensure the correct positioning of test objects, universal holders have been developed for each size of test object. All test samples have a diameter of 45 mm and different thicknesses. The diameters available are 1, 1.5, 2, 2.5, 3, and 3.5 mm. As illustrated in Figure 3, the holder is designed to accommodate test objects with a diameter of 1 mm.

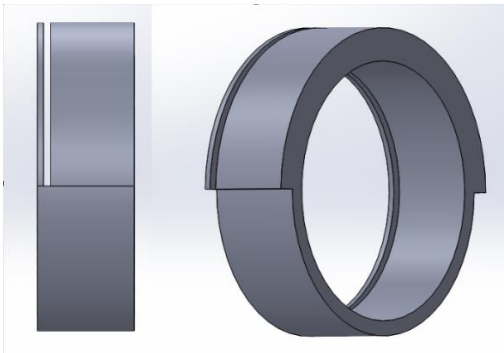

Figure 3. Tested object holder, 1 mm

2.2 Production technology, used material, printing parameters and process conditions

The stand was manufactured by FDM using an Original Prusa MK4S desktop 3D printer (Prusa Research, Prague, Czech Republic) (Figure 4). The MK4S is a Cartesian material-extrusion system in which a direct-drive extruder feeds a thermoplastic filament into a heated liquefier; the molten polymer is extruded through a nozzle and deposited along G-code–defined toolpaths onto a heated build plate, and the three-dimensional part is formed by successive layer-by-layer deposition as the build plate is incrementally lowered along the ZZ axis [11-13]. This working principle is consistent with standard descriptions of FFF for PLA-based materials [11, 14, 15].

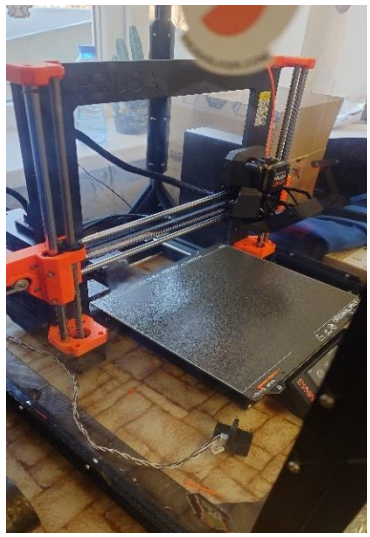

Figure 4. Prusa MK4S

A commercial PLA filament with a nominal diameter of 1.75 mm is used as feedstock, in line with previous studies on PLA FFF and Prusa-ecosystem materials [16, 17]. Unless otherwise stated, a 0.4 mm brass nozzle is employed, which is the standard configuration for desktop PLA FDM and is widely used in dimensional-accuracy and surface-quality studies [12, 14, 18]. The PLA datasheet is shown in Table 1.

Table 1. Properties of polylactic acid (PLA) [19]

Properties of 3D Printed Samples	PLA
Tension module [GPa]	3.3
Tensile strength [MPa]	59.0
Deformation at break (tensile) [%]	4.2
Deformation under tensile strength [%]	3.8
Bending module [GPa]	2.8
Bending strength [MPa]	73.6
Bending deformation at bending strength [%]	3.3
Deformation at break (bending) [%]	3.3

Slicing is performed using PrusaSlicer (Prusa Research 2.9.4), generating G-code for the MK4S. Parts are printed at a nozzle temperature of 220 °C and a bed temperature of 60 °C, with a layer height of 0.150 mm and a nominal print speed of 100 $mm \cdot s^{-1}$. These values fall within the process windows commonly reported for PLA on Prusa MK4-class and comparable FFF printers, where good dimensional accuracy and surface quality are obtained at nozzle temperatures of approximately 200–230 °C, bed temperatures around 50–

65 °C, and print speeds in the range of 20–50 mm·s^{-1} [17, 18, 20, 21].

The extrusion flow rate is as recommended in the slicer, the infill density of 15% using a “Grid” infill pattern. A part-cooling fan duty cycle from 0% to 70% is applied from the first layer to the third one, consistent with common PLA printing practice for balancing interlayer bonding and geometric fidelity [11, 12, 21]. The first layer is printed with 0% fan speed with a slightly increased extrusion width to promote adhesion, and automatic mesh bed leveling and ZZ-offset calibration routines of the MK4S firmware are used before each build to ensure consistent first-layer thickness and contact, as recommended in prior FFF calibration and optimization work [15]. The chosen combination of nozzle diameter, layer height, speeds, and temperatures is in line with parameter sets previously shown to yield high dimensional accuracy and good surface finish in PLA FDM [2, 14, 18, 20, 21].

2.3 Main components

The Nano ESP32 (Figure 5) integrates the ESP32-S3 with the Arduino and MicroPython programming environments. Whether one is a novice embarking on the realm of IoT or MicroPython or an advanced user seeking to integrate it into their subsequent product, the Nano ESP32 emerges as the optimal selection. The software has been designed to cover all the necessary aspects to facilitate the initiation of an IoT or MicroPython project [22]. The term "ESP" is defined as a platform that is open-source and developed for the purpose of facilitating the creation of an extensive range of interactive projects and embedded systems. The integration of hardware and software components facilitates straightforward device creation, which is endowed with the capacity to interact with its environment through the use of control buttons and sensors. The core board is equipped with a microcontroller board and an integrated power supply block, which functions as a central processing module. A variety of sensors, encompassing both analogue and digital types, furnish the controller with the requisite input data for subsequent analysis. Programming is conducted within the specialised Arduino Integrated Development Environment (IDE). A salient benefit of the ESP platform is its ease of use and accessibility for novice users, while concurrently providing adequate flexibility and a wide variety of possibilities to satisfy the requirements of more sophisticated users. The ESP ecosystem has gained significant traction among hobbyists, educators and engineers, largely due to the pervasive availability of free-source libraries and the affordability of the necessary hardware [22].

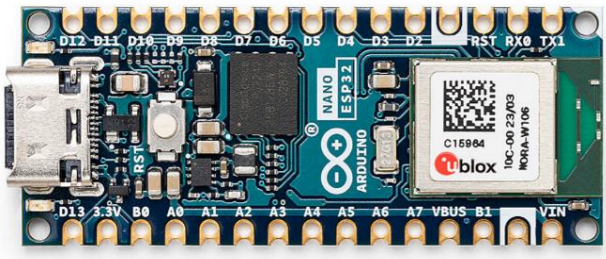

Figure 5. Arduino Nano ESP32

The INA219 (see Figure 6) is a power monitor and a high-side current shunt that features an I^{2}C interface. The INA219 is a multifaceted instrument capable of monitoring both shunt drop and supply voltage, with programmable conversion times and filtering capabilities. The utilisation of a programmable calibration value, in conjunction with an internal multiplier, facilitates direct amperage readings. It is important to note that an additional multiplying register is employed for the purpose of calculating power in watts. The I^{2}C interface is distinguished by its capacity for 16 programmable addresses. The INA219 is designed to detect variations in shunts on buses, with a range spanning from 0 V to 26 V. The device utilises a single +3 V to +5.5 V supply, with a maximum draw of 1 mA of supply current. The INA219 operates within a temperature range of –40 °C to +125 °C [23].

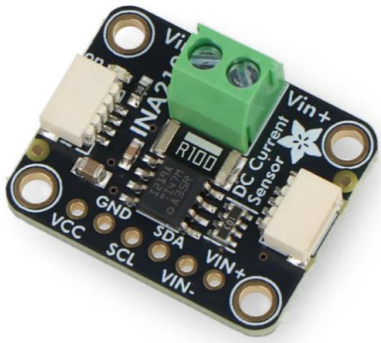

Figure 6. INA219 schematic module

The BHI1750FVI (see Figure 7) is a digital light intensity sensor with an I^{2}C interface and output that can be directly read in lux (lx).

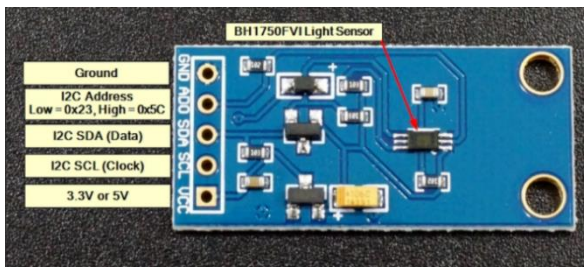

Figure 7. BH1750FVI light sensor

The key features of this light sensor are:

- Visible light measurement. The complete range extends from approximately 400 nm to 700 nm
- 1–65535 lx range
- Wide angle of sensitivity: ± 45 degrees
- Compatible with the majority of the white light sources
- The I^{2}C interface can read the results in lux (lx)

The sensor has been engineered to detect the light spectrum that is visible to the human eye. It exhibits peak sensitivity at 560 nm, which is located within the green spectrum. The full range of the spectrum under consideration spans approximately 400 nm to 700 nm. The sensor demonstrates a high level of functionality when employed in conjunction with a wide range of white visible light sources, encompassing the sun, incandescent lighting, fluorescent lighting, halogen lighting, and white LED lighting. The product has been demonstrated to exhibit effective UV and IR rejection properties [24].

The DS18B20 (see Figure 8) is a digital thermometer that provides measurements in the range of 9 to 12 bits in the Celsius scale. It is equipped with an alarm function and offers user-programmable upper and lower trigger points. These parameters can be configured as per the user's preference. The DS18B20 employs a 1-Wire bus for data communication, which, by definition, necessitates only a single data line (and ground) for interaction with a central microprocessor. Furthermore, the DS18B20 has the capacity to derive power directly from the data line, a process referred to as "parasite power," thereby obviating the necessity for an external power supply. Each DS18B20 possesses a unique 64-bit serial code, a feature that facilitates the concurrent operation of multiple DS18B20s on a single 1-Wire bus. Consequently, it is straightforward to utilise a single microprocessor to regulate multiple DS18B20s dispersed over a substantial area. The system utilises two sensors: one to monitor the temperature of the ice light source and the other to monitor the ambient temperature. Following a comprehensive analysis of the readings obtained, a decision is reached concerning the optimal operating mode for the ice light source fan [25].

Figure 8. DS18B20 temperature sensor

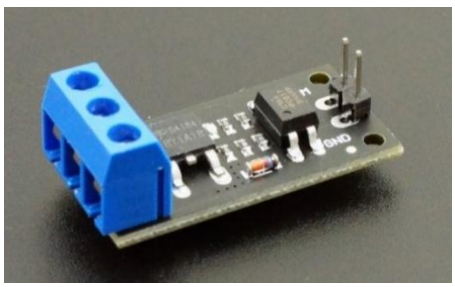

Figure 9. D4184 MOSFET module

The MOSFET module with optoisolation employs the D4184 (see Figure 9) N-Channel logic-compatible MOSFET, which possesses a low Rds(on) and is thus suited to moderate to higher current low-side switching applications. The module incorporates a PC817 optoisolator, which functions as an electrical isolator between the high-powered MOSFET side and the logic signals employed for the control of the module. In the event of a malfunction, the MOSFET should not cause any damage to the microcontroller unit (MCU) being utilised for control purposes. The MCU PWM input to the module drives the internal LED side of the optoisolator. This input comprises a 1 K ohm series current-limiting resistor, the function of which is to ensure that the current through the light-emitting diode (LED) remains within safe levels. This, in turn, enables the input to be driven by a maximum of 20 volts, or even higher in the absence of a MCU. In the event of a low or disconnected PWM input signal, the internal LED in the optoisolator is deactivated. Consequently, this results in the phototransistor output being disabled. With the phototransistor deactivated, the MOSFET gate is pulled to ground by a 4.7 K resistor. This results in the MOSFET being turned off, thereby disconnecting the load from ground and disabling it. The activation of the internal optoisolator LED is initiated by a logic high on the PWM input, which subsequently leads to the activation of the phototransistor. This configuration results in the formation of a voltage divider, which is predominantly composed of two 4.7 K resistors. The application of a bias of 50% of the power supply voltage to the gate results in the activation of the MOSFET. In the event of a 12 V power supply being utilised, the gate will be at 6 V. The diode is believed to be a 12 V Zener diode that limits the gate voltage of the MOSFET to a safe level [26].

LEDs exhibit virtually zero warm-up time, thereby producing maximum brightness instantaneously due to their utilisation of electroluminescence as opposed to filament heating. Whilst the activation of the LEDs occurs instantaneously, it is important to note that LED drivers can induce a negligible millisecond delay, which is imperceptible to the human observer. Although the system requires up to 30 minutes to reach full thermal equilibrium, it can be considered in a steady state under the tested conditions due to the low current draw and the light source's stable operating temperature, which matches the ambient laboratory temperature.

3. RESULTS AND DISCUSSION

ASTM D1003 is a standard method for measuring the light transmittance of plastics. Typically, open-type measuring instruments are used for this method (ASTM, 2019). ISO 13468 is a standard for measuring total light transmittance in the visible spectrum. The proposed stand utilises the measurement concept outlined in these standards; however, it has been designed as a closed-type system, thereby eliminating the influence of external light noise. A laboratory stand is developed using additive printing technology based on the materials and methods presented in Figure 10. The basic principles presented are followed during its construction. A special holder is created for each sample size, ensuring precise positioning between the light source, sample, and light sensor.

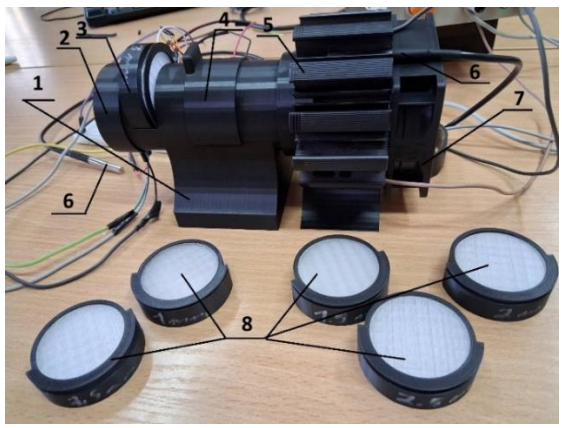

Figure 10. The stand in a laboratory environment

The stand comprises: (1) a base; (2) a light-sensor cover with a concealed sensor; (3) a holder for the test specimen; (4) a movable cover for enclosing the specimen during measurement; (5) a cooler assembly with an integrated light source; (6) temperature sensors; (7) a cooling fan for the light

source; and (8) auxiliary holders and accessories.

The stand is controlled by an ESP32 controller. Measuring modules for optical and electrical quantities, temperature sensors, and PWM control modules are interfaced with the controller. The electronic components of the stand are operated and measurement data is collected through a program code developed specifically for this purpose in the Arduino IDE environment. Additionally, the automated acquisition reduces operator-dependent variability and enhances the reproducibility of measurements [27]. The measurement workflow follows the block diagram shown in Figure 11.

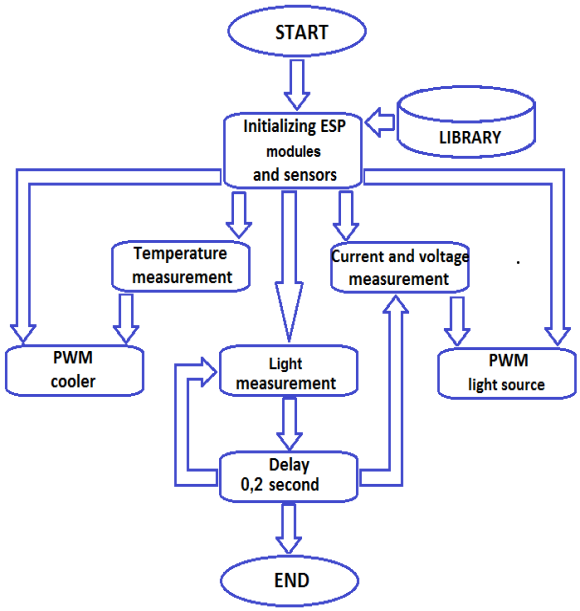

Figure 11. Measurement procedure block scheme

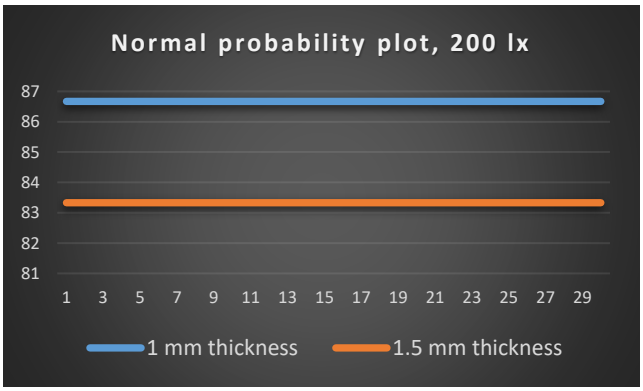

Figure 12. Normal distribution plot, 200 lx

The process begins with booting the system and loading the main software and the necessary libraries for the peripheral modules. Then, while monitoring and controlling the operating temperature of the source and the electrical parameters, the procedure for measuring and calibrating the stand begins. Calibration is performed with no test sample in the stand. The calibration steps are repeated each time the sample or the light intensity received from the source changes. The light source intensity is controlled by monitoring the electrical parameters. Once the calibration process is complete and the measured values are stable, the transmittance of the samples under investigation can be measured. The selected test detail is placed in the holder (Figure 12) and then in the stand. The movable cover is closed, and the measurement procedure (Figure 11) is performed. The obtained data is entered into tables, and the results are presented graphically. Due to the specificity and short duration of the measurement, multiple measurements are performed. The measurement data is checked for compliance with the normal distribution law using the Anderson–Darling (AD) test, the Shapiro–Wilk test, or another similar method. A test for gross errors (Grubbs' test) is also performed. If the data follow the normal distribution law and there are no gross errors, the transmittance and light attenuation are calculated according to the test sample. Transmittance is calculated as the difference between the illuminance during calibration and the illuminance obtained from the measurement with the test sample in place, as shown in Eq. (1). The unit of measurement used for transmittance is lux (lx).

$$\Delta T = T_c - T_m \quad (1)$$

where,

ΔT: Transmittance difference;

T_c: calibration Transmittance;

T_m: measured transmittance with a test element in place.

Attenuation is calculated as the ratio between transmittance and calibration value, with the results expressed as a percentage (%).

$$\delta_{la} = \frac{\Delta E}{Ec} \cdot 100\% \quad (2)$$

where,

δ_{la}: light attenuation;

ΔE: transmittance;

E_c: calibration illuminance.

To validate the stand and demonstrate its capabilities, data from measurements of samples with thicknesses of 1 mm, 1.5 mm, 2 mm, 2.5 mm, 3 mm and 3.5 mm are presented. All test samples are produced using the same printing parameters; only the thickness of the sample varies. Tests are performed on test samples of the aforementioned thicknesses at calibration illuminance levels ranging from 200 lx to 10,600 lx in increments of 800 lx. Due to the large volume of data, only the results at the following calibration illuminance levels are presented: 200 lx, 2,600 lx, 6,600 lx and 10,600 lx. Table 2 shows the results of measuring samples with thicknesses of 1 mm and 1.5 mm at 200 lx, with 30 measurements taken for each sample. The values of voltage (V), current (A), and light (lx) are also indicated. During the measurements, the temperature sensors do not detect any change in the temperature of the light source. The measured temperature of the light source is 25 degrees. The standard deviation, repeatability error, and measurement uncertainty were calculated for the presented data (see Table 3).

Table 2. 1 mm and 1.5 mm light measurements data

No.	1 mm			1.5 mm		
	V	mA	lx	V	mA	lx
1	7.88	4.7	86.67	7.88	4.6	83.33
2	7.88	4.7	86.67	7.88	4.5	83.33
3	7.87	4.4	86.67	7.88	4.6	83.33
4	7.87	4.6	86.67	7.87	4.4	83.33
5	7.88	4.4	86.67	7.88	4.8	83.33
6	7.87	4.4	86.67	7.88	4.4	83.33
7	7.88	4.5	86.67	7.88	4.6	83.33
8	7.88	4.3	86.67	7.88	4.5	83.33
9	7.88	4.6	86.67	7.88	4.4	83.33

10	7.87	4.7	86.67	7.88	4.4	83.33
11	7.88	4.6	86.67	7.87	4.7	83.33
12	7.88	4.5	86.67	7.88	4.7	83.33
13	7.88	4.6	86.67	7.88	4.4	83.33
14	7.88	4.4	86.67	7.88	4.6	83.33
15	7.88	4.8	86.67	7.87	4.4	83.33
16	7.88	4.4	86.67	7.87	4.4	83.33
17	7.87	4.6	86.67	7.88	4.5	83.33
18	7.88	4.5	86.67	7.87	4.3	83.33
19	7.87	4.4	86.67	7.88	4.6	83.33
20	7.88	4.4	86.67	7.88	4.7	83.33
21	7.88	4.7	86.67	7.88	4.4	83.33
22	7.88	4.5	86.67	7.87	4.4	83.33
23	7.88	4.5	86.67	7.88	4.5	83.33
24	7.87	4.7	86.67	7.87	4.3	83.33
25	7.88	4.5	86.67	7.88	4.6	83.33
26	7.88	4.5	86.67	7.88	4.7	83.33
27	7.88	4.4	86.67	7.88	4.6	83.33
28	7.87	4.4	86.67	7.88	4.5	83.33
29	7.88	4.4	86.67	7.87	4.6	83.33
30	7.88	4.3	86.67	7.88	4.4	83.33

Table 3. Statistical check

	1 mm	1.5 mm
Sample Standard Deviation	2.89×10^{-14}	2.89×10^{-14}
Uncertainty, lx	5.22×10^{-15}	5.22×10^{-15}
Repeatability error, lx	3.33×10^{-16}	3.46×10^{-16}
Repeatability error, %	3.33×10^{-14}	3.46×10^{-14}

The results presented in Table 2 show insignificant changes in the voltage and current values, as well as identical light measurement values. Figure 12 shows the data distribution, as shown in the graph; all the data is grouped in a straight line. Based on these results, only the average values from the remaining measurements are shown, since the fluctuations in the data are similar. Table 4 shows the measurement data for all sample thicknesses at calibration light levels of 200 lx, 2,600 lx, 6,600 lx and 10,600 lx. Transmittance is calculated using Eq. (1).

Table 4. Light transmittance data of all tested objects

Thickness, mm	200 lx	2600 lx	6600 lx	10600 lx
1.0	86.67	1162.69	2909.88	4743.76
1.5	83.33	1056.59	2668.74	4475.21
2.0	60.00	785.74	2028.09	3230.45
2.5	56.67	725.88	1863.47	2995.23
3.0	49.17	674.74	1713.069	2754.88
3.5	46.67	649.15	1618.26	2596.18

Table 5. Light attenuation

Thickness, mm	Attenuation, %			
	200	2600	6600	10600
1.0	56.66	55.28	55.91	55.25
1.5	58.33	59.36	59.56	57.78
2.0	70.00	69.78	69.27	69.52
2.5	71.66	72.08	71.77	71.74
3.0	75.41	74.05	74.04	74.01
3.5	76.66	75.03	75.48	75.51

Table 5 shows the light attenuation calculated using Eq. (2).

The results obtained for light attenuation show very similar values (less than 2% difference) for each of the samples at different light intensities.

To make the results easier to understand, three graphs showing the relationship between attenuation and illuminance (Figure 13), illuminance and sample thickness (Figure 14), and illuminance and sample thickness (Figure 15) are presented.

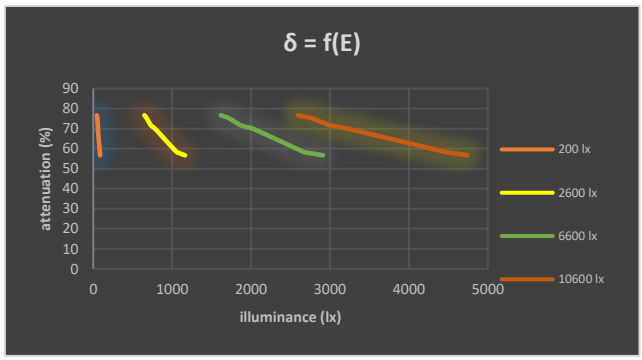

Figure 13. Attenuation to illuminance

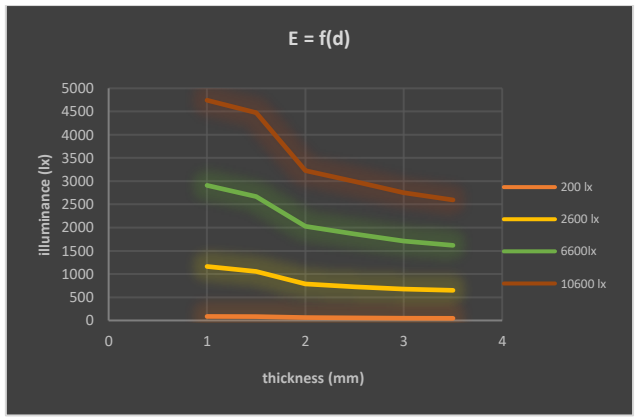

Figure 14. Illuminance to thickness

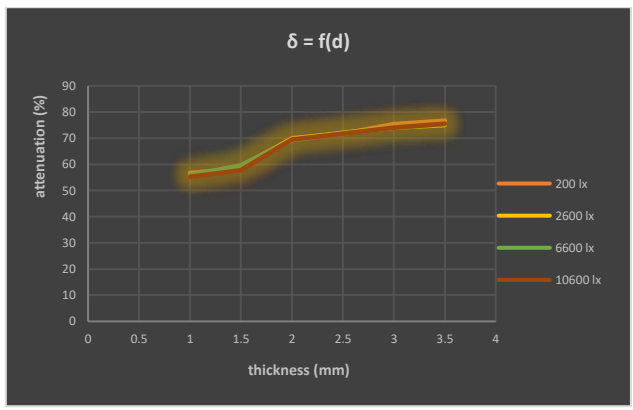

Figure 15. Attenuation to thickness

According to the obtained results, the transmittance of the sample decreases as its thickness increases. This condition is valid for all the presented measurement conditions. The attenuation percentage is independent of illuminance. As shown in Figure 13, the relationship between attenuation and illuminance is linear. The differences in attenuation values at various light levels are minimal, never exceeding 2%. This indicates that lighting has little impact on attenuation percentages. This confirms that the material being measured exhibits stable optical properties within the considered light range. Figure 14 shows the relationship between illuminance and the thickness of the test samples. A step change in the relationship between thickness and detail is observed at 1.5 mm. After a sample thickness of 2 mm, the relationship

becomes linear. At the lowest illuminance, the step is least pronounced; as the illuminance increases, however, this relationship becomes increasingly pronounced. The occurrence of this specific zone can be attributed to the attainment of a critical thickness, at which the internal structure of the material begins to exert a more substantial influence on the propagation of light. This phenomenon warrants further in-depth research to establish this dependence. Figure 15 shows the attenuation with respect to the thickness of the details. It shows that attenuation depends strongly on the thickness of the test detail. The curves for different illuminances practically overlap, which once again confirms the hypothesis that attenuation is mainly a function of thickness rather than illuminance. Increasing the thickness of the material results in an increased optical path length, which consequently leads to higher losses due to absorption and scattering.

4. CONCLUSIONS

The stand demonstrates good performance and high repeatability of results. Its modular design allows the main components to be replaced quickly and easily. It enables research to be conducted using different types of light sources. Its specific features allow it to be used in teaching various engineering science disciplines. Individual holders for the test samples ensure the test details can be replaced quickly and easily, and guarantee uniform conditions during measurement. Experimental data reveal the relationships between the studied quality indicators, the thickness of the samples and the level of illumination. The findings demonstrate that illumination exerts minimal influence on the attenuation rate, as evidenced by the negligible disparities observed between the curves. The observed transition from 1.5 mm to 2 mm is indicative of a structural or optical modification in the material, which is a subject of interest for future, more in-depth research. Due to the wide variety of semi-transparent materials used in additive manufacturing, more experiments are needed with different types of semi-transparent materials and manufacturing modes. In its current configuration, the test stand is capable of measuring overall light transmittance, which could be considered a limitation. Plans are in place to integrate a spectroscopy sensor, which would add additional functionality and enable more in-depth analyses.

ACKNOWLEDGMENT

The authors would like to thank the Research and Development Sector at the Technical University of Sofia for the financial support.

REFERENCES

[1] Wang, C., Zhou, Z.Y. (2023). Optical properties and lampshade design applications of PLA 3D printing materials. Bioresources, 18(1): 1545-1553. https://doi.org/10.15376/biores.18.1.1545-1553

[2] Vochozka, V., Černý, P., Šramhauser, K., Špalek, F., Kříž, P., Čech, J., Zoubek, T., Bartoš, P., Kresan, J., Stehlík, R. (2024). Fused filament fabrication 3D printing parameters affecting the translucency of polylactic acid parts. Polymers, 16(20): 2862. https://doi.org/10.3390/polym16202862

[3] Hamp, S.M., Logan, R.D., Shaw, J.A. (2021). Optical transmittance of 3D printing materials. Applied Optics, 60(22): 6573-6578. https://doi.org/10.1364/AO.427525

[4] Shahpaski, M., Sapaico, L.R., Süsstrunk, S. (2019). Comparative analysis of transmittance measurement geometries and apparatus. Electronic Imaging, 31: art00006. https://doi.org/10.2352/ISSN.2470-1173.2019.6.MAAP-477

[5] Hwang, J., Baek, Y. (2025). Spectrophotometer-employed method for measuring luminous transmittance and haze. Metrologia, 62(6): 065005. https://doi.org/10.1088/1681-7575/ae21e4

[6] Liu, W.C., Koo, A., Molloy, E., Wu, H., Leecharoen, R., Zhang, J., Liu, Y., Suryani, D., Yu, H.L. (2024). APMP pilot study on high transmittance haze. Journal of Physics: Conference Series, 2864: 012011. https://doi.org/10.1088/1742-6596/2864/1/012011

[7] Simonot, L., Hébert, M., Mazauric, S., Hersch, R.D. (2017). Assessing the proper color of translucent materials by an extended two-flux model from measurements based on an integrating sphere. Electronic Imaging 29: art00008. https://doi.org/10.2352/ISSN.2470-1173.2017.8.MAAP-291

[8] Abu Rmaileh, L., Nguyen, P., Kissel, A., Urban, P. (2025). Determining intrinsic optical properties of 3D printing materials. Optics Express, 33(13): 28493-28510. https://doi.org/10.1364/OE.559881

[9] Pranovich, A., Hannemose, M.R., Jensen, J.N., Tran, D.M., Aanæs, H., Gooran, S., Nyström, D., Frisvad, J.R. (2024). Digitizing the appearance of 3D printing materials using a spectrophotometer. Sensors, 24(21): 7025. https://doi.org/10.3390/s24217025

[10] da Cruz Junior, L.B., Bachmann, L. (2021). Manufacture and characterization of a 3D-printed integrating sphere. Instrumentation Science & Technology, 49(3): 276-287. https://doi.org/10.1080/10739149.2020.1824922

[11] Liao, Y., Liu, C., Coppola, B., Barra, G., Di Maio, L., Incarnato, L., Lafdi, K. (2019). Effect of porosity and crystallinity on 3D printed PLA properties. Polymers, 11(9): 1487. https://doi.org/10.3390/polym11091487

[12] Mendricky, R., Fris, D. (2020). Analysis of the accuracy and the surface roughness of FDM/FFF technology and optimisation of process parameters. Tehnički Vjesnik, 27(4): 1166-1173. https://doi.org/10.17559/TV-20190320142210

[13] Patel, S.Y., Desai, C.K. (2024). Effect of layer height on tensile strength of fused deposited modeling printed carbon poly-lactic acid part. International Journal of Scientific Research in Engineering and Management, 8(8): 1-6. https://doi.org/10.55041/ijsrem37009

[14] García Plaza, E., Núñez López, P.J., Caminero Torija, M.Á., Chacón Muñoz, J.M. (2019). Analysis of PLA geometric properties processed by FFF additive manufacturing: Effects of process parameters and plate-extruder precision motion. Polymers, 11(10): 1581. https://doi.org/10.3390/polym11101581

[15] Grubbs, J., Sousa, B.C., Cote, D.L. (2023). Establishing a framework for fused filament fabrication process optimization: A case study with PLA filaments. Polymers, 15(8): 1945. https://doi.org/10.3390/polym15081945

[16] Orellana-Barrasa, J., Tarancón, S., Pastor, J.Y. (2023). Effects of accelerating the ageing of 1D PLA filaments after fused filament fabrication. Polymers, 15(1): 69. https://doi.org/10.3390/polym15010069
[17] Wang, S., D'hooge, D.R., Daelemans, L., Xia, H., Clerck, K.D., Cardon, L. (2020). The transferability and design of commercial printer settings in PLA/PBAT fused filament fabrication. Polymers, 12(11): 2573. https://doi.org/10.3390/polym12112573
[18] Luis-Pérez, C.J., Buj-Corral, I., Sánchez-Casas, X. (2021). Modeling of the influence of input AM parameters on dimensional error and form errors in PLA parts printed with FFF technology. Polymers, 13(23): 4152. https://doi.org/10.3390/polym13234152
[19] AzureFilm. Technical data sheets. https://azurefilm.com/wpcontent/uploads/2023/10/PLA_TDS.pdf, accessed on Apr. 23, 2026.
[20] Li, Y., Molazem, A., Kuo, H.I., Ahmadi, V., Shastri, V.P. (2025). Comparative analysis of dimensional accuracy in PLA-based 3D printing: Effects of key printing parameters and related variables. Polymers, 17(12): 1698. https://doi.org/10.3390/polym17121698
[21] Abas, M., Habib, T., Noor, S., Salah, B., Zimon, D. (2022). Parametric investigation and optimization to study the effect of process parameters on the dimensional deviation of fused deposition modeling of 3D printed parts. Polymers, 14(17): 3667. https://doi.org/10.3390/polym14173667
[22] Babiuch, M., Foltýnek, P., Smutný, P. (2019). Using the ESP32 microcontroller for data processing. In 2019 20th International Carpathian Control Conference (ICCC), Krakow-Wieliczka, Poland, pp. 1-6. https://doi.org/10.1109/carpathiancc.2019.8765944
[23] Lambert, J., Monahan, R., Casey, K. (2021). Power consumption profiling of a lightweight development board: Sensing with the INA219 and Teensy 4.0 microcontroller. Electronics, 10(7): 775. https://doi.org/10.3390/electronics10070775
[24] Burjes, A.Y., Najm, H.Y., Ahmad, S.M. (2022). Design and executing automatic solar tracking system (ASTS) based on Arduino-Mega and light intensity sensor GY-30. ResearchJet Journal of Analysis and Inventions-RJAI, 3(8).
[25] Gaspar, G., Dudak, J., Mikolajcikova, M., Gurin, D. (2023). Proposal of a skin temperature measurement system based on digital thermometers. IEEE Access, 11: 25050-25062. https://doi.org/10.1109/access.2023.3255511
[26] Nahrendra, I.M.A., Adiprawita, W., Susanto, A., Hadinata, S. K. (2018). Engine control unit for 2 stroke internal combustion engine on medium altitude unmanned aerial vehicle. In 2018 International Symposium on Electronics and Smart Devices (ISESD), Bandung, Indonesia. https://doi.org/10.1109/isesd.2018.8605492
[27] Mitev, P., Tashev, A., Stoyanov, Y. (2025). Design and construction of an engine oil viscosity meter with electronic control. Engineering Proceedings, 100(1): 55. https://doi.org/10.3390/engproc2025100055

NOMENCLATURE

AM	Additive manufacturing
FDM	Fused deposition modeling
FFF	Fused filament fabrication
ASTM	American Society for Testing and Materials
PLA	Polylactic acid
ISO	International Organization for Standardization
LED	Light-emitting diode
GPa	Gigapascal, pressure, 10^9 Pa
MPa	Megapascal, pressure, 10^6 Pa
V	Voltage, volts
A	Current, amper
I^2C	Communication protocol
lx	Illuminance unit, lux
nm	Nanometer, 1.10^{-9} meter
UV	Ultraviolet light
IR	Infrared light
MCU	Microcontroller unit
PWM	Pulse-Width Modulation
E_c	Calibration illuminance, lx
E_m	Measured illuminance with a test element, lx
ΔE	Transmittance, lx

Greek symbols

°	Angle measurement, degree
ø	Diameter, mm
°C	Degree Celsius
Δ	Difference
δ_{la}	Light attenuation, %

Subscripts

c	Calibration
m	Measured illuminance
la	Light attenuation